

Physical characterization of the FeLoBAL outflow in SDSS J0932+0840: Analysis of VLT/UVES observations

Mayank Sharma^{1,*}, Nahum Arav¹, Kirk T. Korista², Manuel Bautista², Maryam Dehghanian¹,
Doyee Byun^{1,3}, Gwen Walker¹, and Sasha Mintz¹

¹ Department of Physics, Virginia Tech, Blacksburg, VA 24061, USA

² Department of Physics, Western Michigan University, 1120 Everett Tower, Kalamazoo, MI 49008-5252, USA

³ Department of Astronomy, University of Michigan, Ann Arbor, MI, 48109, USA

Received October 24, 2024; accepted December 9, 2024

ABSTRACT

Context. The study of quasar outflows is essential in understanding the connection between active galactic nuclei (AGN) and their host galaxies. We analyze the VLT/UVES spectrum of quasar SDSS J0932+0840 and identify several narrow and broad outflow components in absorption, with multiple ionization species including Fe II, which puts it among a rare class of outflows known as FeLoBALs.

Aims. We study one of the outflow components to determine its physical characteristics by determining the total hydrogen column density, ionization parameter and the hydrogen number density. Through these parameters, we aim to obtain the distance of the outflow from the central source, its mass outflow rate and kinetic luminosity, and to constrain the contribution of the outflow to AGN feedback.

Methods. We obtain the ionic column densities from the absorption troughs in the spectrum, and use photoionization modeling to extract the physical parameters of the outflow, including the total hydrogen column density and ionization parameter. The relative population of the observed excited states of Fe II is used to model the hydrogen number density of the outflow.

Results. We use the Fe II excited states to model the electron number density (n_e) and hydrogen number density (n_H) independently and obtain $n_e \approx 10^{3.4} \text{ cm}^{-3}$ and $n_H \approx 10^{4.8} \text{ cm}^{-3}$. Our analysis of the physical structure of the cloud shows that these two results are consistent with each other. This places the outflow system at a distance of $0.7^{+0.9}_{-0.4}$ kpc from the central source, with mass flow rate (\dot{M}) of $43^{+65}_{-26} M_\odot \text{ yr}^{-1}$ and kinetic luminosity (\dot{E}_k) of $0.7^{+1.1}_{-0.4} \times 10^{43} \text{ erg s}^{-1}$. This is $0.5^{+0.7}_{-0.3} \times 10^{-4}$ of the Eddington luminosity (L_{Edd}) of the quasar and we thus conclude that this outflow is not powerful enough to contribute significantly towards AGN feedback.

Key words. Galaxies: active – Galaxies: evolution – Galaxies: kinematics and dynamics – Quasars: absorption lines – Quasars: individual: SDSS J093224.48-084008.0

1. Introduction

Quasar outflows, detected as blue-shifted absorption troughs relative to the systemic redshift of the active galactic nuclei (AGN), are observed ubiquitously. They are invoked as the primary mechanism in the quasar mode of AGN feedback, and may play an important role in the evolution of the supermassive black hole (SMBH) (e.g., Silk & Rees 1998; Begelman & Nath 2005; Hopkins et al. 2009; Liao et al. 2024), evolution of the host galaxy (e.g., Di Matteo et al. 2005; Ostriker et al. 2010; Choi et al. 2017; Cochrane et al. 2023), enrichment of the intergalactic medium (e.g., Moll et al. 2007; Fabjan et al. 2010; Ciotti et al. 2022) and cooling flows in clusters of galaxies (e.g., Begelman & Ruszkowski 2005; Brüggén & Scannapieco 2009; Hopkins et al. 2016; Weinberger et al. 2023).

Based on the width of the detected absorption lines (defined as continuous absorption with normalized flux < 0.9), quasar outflows are commonly classified into one of the three following categories. Broad absorption lines (BALs) are defined as having velocity width $\Delta v \gtrsim 2000 \text{ km s}^{-1}$, and are found in $\sim 20\%$ of quasar spectra (Weymann et al. 1991; Hewett & Foltz 2003; Reichard et al. 2003; Knigge et al. 2008), mini-BALs have velocity widths $500 \lesssim \Delta v \lesssim 2000 \text{ km s}^{-1}$ and an incidence rate of $\sim 10\%$ (Hamann & Sabra 2004; Hidalgo et al. 2012; Moravec

et al. 2017; Chen et al. 2021), and finally narrow absorption lines (NALs) with velocity width $\Delta v \lesssim 500 \text{ km s}^{-1}$ are the most common and detected in $\sim 60\%$ of quasar spectra (Vestergaard 2003; Ganguly & Brotherton 2008; Stone & Richards 2019).

BAL quasar (BALQSO) outflows have been further classified into three categories based on the ionization state of the observed absorption lines in their spectra (Hall et al. 2002). High-ionization BALQSOs (HiBALs) show absorption from only high ionization species, such as C IV, Si IV, N V and O VI, and are the most common, being observed in all BALQSOs. (Voit et al. 1993; Dai et al. 2012). Low-ionization BALQSOs (LoBALs) show absorption lines from the high ionization species, but are also accompanied by lower ionization species such as Mg II, C II and Al III, and are observed in $\sim 10\%$ of BALQSOs (Weymann et al. 1991; Trump et al. 2006). Belonging to the rarest class are iron low-ionization BALQSOs (FeLoBALs), showing absorption from both high and low ionization species along with Fe II or Fe III, making up just $\sim 0.3\%$ of the quasar population (Trump et al. 2006).

Theoretically, these classifications for quasar outflows are understood through two different models. In the context of an orientation based model, BALQSOs are observed as a result of the intersection of our line of sight with outflowing gas that is launched from a narrow range of radii on the accretion disk (Murray et al. 1995; Elvis 2000). The different ionization sub-

* e-mail: mayanksh@vt.edu

classes then relate to the column density of the material they encounter, with HiBALS having the smallest column and FeLoBALs having the largest, extending beyond the H II region (Arav et al. 2001b; Korista et al. 2008; Lucy et al. 2014). The opening angle for such a line of sight would be small (Green et al. 2001; Gallagher et al. 2006; Morabito et al. 2011), thus explaining the rarity of FeLoBALs. An alternative evolutionary model suggests that FeLoBALs might represent a short-lived phase in which a young quasar is observed in the process of breaking through a cocoon of enveloping dust and gas (Voit et al. 1993).

FeLoBALs usually show a plethora of absorption troughs from ground state and various excited state transitions, which makes them an excellent diagnostic of the physical state of the outflowing gas. Arav et al. (2001a); de Kool et al. (2001, 2002a,b) presented some of the first detailed photoionization analysis of FeLoBAL quasars by utilizing Keck HIRES spectra and obtained constraints on the temperature, ionization parameter (U_H), electron number density (n_e) and distance from the emission source (R) for the outflows. Korista et al. (2008); Arav et al. (2008); Moe et al. (2009); Dunn et al. (2010); Bautista et al. (2010) utilized high resolution and signal to noise spectra (from Very Large Telescope (VLT) and Astrophysical Research Consortium telescope (ARC)). This allowed them to improve upon the accuracy of the column density and number density measurements and obtain mass flux and kinetic luminosity for some outflows, thus constraining the extent of their contribution to AGN feedback processes. Leighly et al. (2018) introduced the novel spectral-synthesis procedure *SimBAL*, which has led to an impressive increase in the number of FeLoBALs that have been subjected to a detailed spectral analysis. Choi et al. (2022b) presented a *SimBAL* analysis of 50 low-redshift FeLoBAL quasars that cover a wide range in the parameter space for U , n_e and R , and introduced a new class of loitering FeLoBAL outflows. Choi et al. (2022a) and Leighly et al. (2022) extended this analysis further to the geometry of the outflows and the optical line emission properties for the host quasars. Other recent studies of individual quasar outflows have led to the discovery of increasingly interesting properties and phenomenon: Choi et al. (2020) discovered a remarkably powerful FeLoBAL outflow with the highest observed velocity and kinetic luminosity; Xu et al. (2021) found differences in the physical conditions for Fe II and Fe III formation in Q0059–2735; Byun et al. (2022a) found the farthest known mini-BAL outflow system at ~ 67 kpc and along with Walker et al. (2022), an extremely high mass outflow rate, capable of contributing significantly to AGN feedback processes.

In this paper, we present a study of the Ultraviolet and Visual Echelle Spectrograph (UVES) spectrum of the quasar SDSS J093224.48+084008.0 (hereafter, J0932+0840), obtained with the Very Large Telescope (VLT). Section 2 describes the observation and how the data for our analysis was obtained. In Section 3, we analyze the spectrum to obtain the column densities of the observed troughs, along with the photoionization modeling of the outflow. Section 4 discusses our diagnostics for the outflow’s electron and hydrogen number densities based on the population of the observed excited states. Section 5 presents the energetics of the outflow. Section 6 discusses the observed variability between the different epochs, along with a re-evaluation of properties from a few previous FeLoBAL studies. Finally, we summarize and conclude the paper in Section 7.

Throughout the paper, we adopt a standard Λ CDM cosmology with $h = 0.677$, $\Omega_m = 0.310$ and $\Omega_\Lambda = 0.690$. (Planck Collaboration et al. 2020).

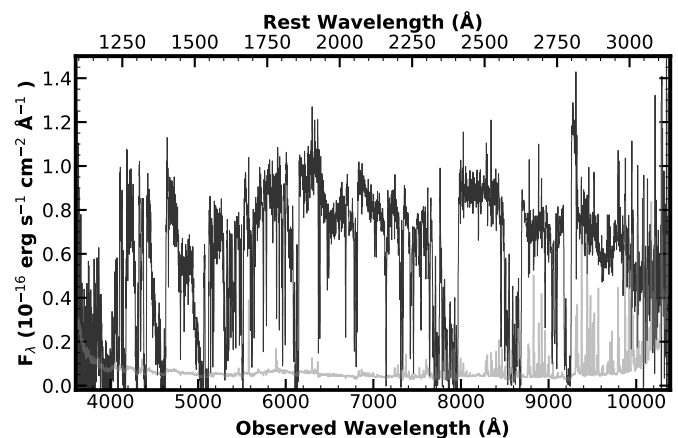


Fig. 1: Unnormalized SDSS spectra of J0932+0840 (2012 epoch). The flux density (F_λ) is shown in black with the error plotted in gray.

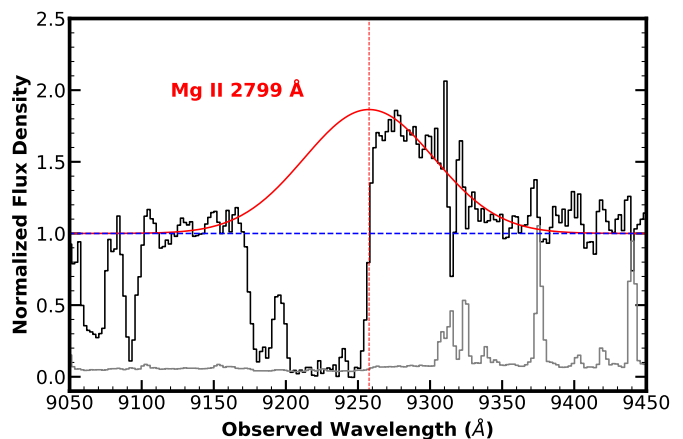


Fig. 2: Gaussian model fit for the Mg II 2799 emission feature (shown in red). Due to heavy absorption, the data points for the fit were selected manually. The red dashed line marks the centroid of the best-fit model which we use to determine the redshift of the quasar. The blue dashed line shows the continuum level. The error in flux is shown in gray.

2. Data overview

2.1. Observation and data acquisition

J0932+0840 (J2000: RA=09:32:24.48; DEC: +08:40:08.0) was observed with VLT/UVES on 30 April, 2008, with a total exposure time of 28.1 ks, as part of program 081.B-0285 (PI: Benn). The data covers a spectral range of 3758–10250 \AA , with resolution $R \approx 48,000$ and an average signal to noise ratio $\text{SNR} \approx 30$ per resolution element. The data was then reduced and normalized by Murphy et al. (2019) as part of the first data release (DR1) of the UVES Spectral Quasar Absorption Database (SQUAD). Fig. 3 shows the obtained normalized data.

J0932+0840 was also observed on two occasions (20 Dec. 2003 and 26 January 2012) as part of the Sloan Digital Sky Survey (SDSS). While our primary analysis is based on the higher resolution and SNR SQUAD data, it lacks information about any emission features as it is normalized. Therefore, we use the SDSS spectrum (Fig. 1) to: (i) obtain the redshift of the quasar (section 2.2), (ii) scale the flux of our SED to obtain the Bolo-

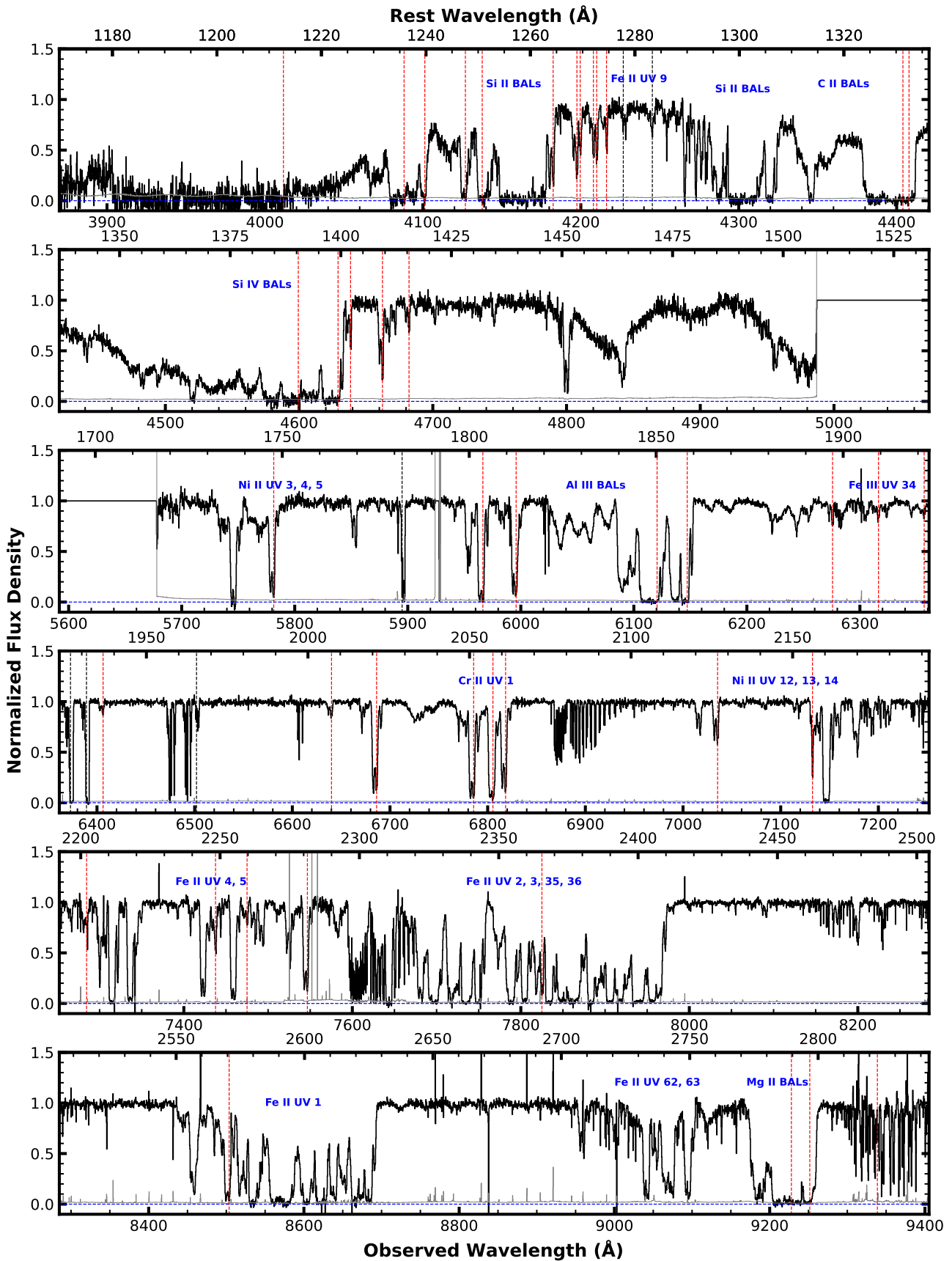


Fig. 3: Normalized UVES spectrum of J0932-0840. Important features and multiplets are marked in blue, and the identified absorption troughs from the primary outflow system at $v \approx -720 \text{ km s}^{-1}$, are marked with red dashed lines. The zero flux level is shown by the blue dashed lines. Black dashed lines mark troughs from an intervening system at $z = 1.28$.

metric luminosity (section 5.1), and, (iii) obtain the black hole mass (section 5.2).

2.2. Redshift determination

The second epoch of SDSS observation (Fig. 1) covers the Mg II $\lambda\lambda$ 2796.35, 2803.53 emission feature which can be utilized to obtain the redshift of the quasar. We first model the underlying continuum emission with a power law, and then the Mg II emission feature is modeled with a single Gaussian, with the result of this fit is shown in Fig. 2. This leads to a redshift of $z = 2.308 \pm 0.001$. This is close to the redshift estimate obtained by Yi et al. (2019) ($z = 2.300$) in their study of 134 Mg II broad absorption-line (BAL) quasars including J0932+0840. We note, however, that these redshift values are in disagreement with the value determined by Hewett & Foltz (2003) ($z = 2.341231 \pm 0.001884$). They determined this value by modeling the 1900 blend, which includes Al III 1857 ($\lambda\lambda$ 1854.72, 1862.78), Si III] 1892 (λ 1892.03) and the C III] 1909 (λ 1908.73) emission lines in the first epoch of SDSS observation, as it does not cover the Mg II emission feature. As this blend includes multiple emission features of similar strengths, it is more prone to uncertainty than the fit obtained for Mg II, and therefore we use $z = 2.308$ for our analysis.

3. Spectral analysis

3.1. Identifying outflow systems

The UVES spectrum of J0932+0840 shows a large number of absorption systems ranging in velocities from -500 to -5000 km s $^{-1}$. The lowest velocity systems (~ -500 , -700 and -850 km s $^{-1}$) are narrow absorption lines ($\Delta v \sim 100$ km s $^{-1}$) and are observed in most species, including both low and high ionization. The higher velocity systems (~ -1300 , -4200 and -5000 km s $^{-1}$) are much broader ($\Delta v \gtrsim 2000$ km s $^{-1}$) falling under the classification of BALs and are only seen in a few species like Si II, C II, Mg II, Al III, Si IV and C IV (the latter is only covered in the SDSS spectrum). The focus of this paper is on the system with velocity ~ -700 km s $^{-1}$ (hereafter S2) as it shows absorption from the most species and is thus rich in diagnostics.

3.2. Column density determination

In order to constrain the physical characteristics of an outflow system, it is important to obtain the column densities of the observed ionic species. For a given ionic transition with rest wavelength λ (in Angstroms) and oscillator strength f , the column density N_{ion} is obtained using (Savage & Sembach 1991):

$$N_{ion} = \frac{m_e c}{\pi e^2 f \lambda} \int \tau(v) dv = \frac{3.8 \times 10^{14}}{f \lambda} \int \tau(v) dv \quad [\text{cm}^{-2}] \quad (1)$$

where m_e is electron mass, c is the speed of light, e is elementary charge and $\tau(v)$ is the optical depth profile for the transition, which is based on the choice of the absorber model. The simplest model, known as the apparent optical depth (AOD) model assumes a homogeneous outflow that completely covers the source. In this case, the normalized intensity profile $I(v)$ is then simply related to $\tau(v)$ as:

$$I(v) = e^{-\tau(v)} \quad (2)$$

This model does not account for partial line of sight (LOS) covering and saturation effects in line centers and can thus underestimate the column densities. Therefore for saturated troughs,

only lower limits to the column densities can be obtained using the AOD model. In the case of J0932+0840, however, we have detected several 'weak' transitions, that have small oscillator strength values. These troughs are much shallower than the other deeper troughs from the same ion and can thus be considered unsaturated. Therefore we regard the derived column densities for these transitions as actual measurements.

If two or more lines from the same lower energy level are detected for an ion, we can employ a more physical inhomogeneous absorber model, where the gas distribution is approximated with a power law (de Kool et al. 2002c; Arav et al. 2005). The optical depth profile within the outflow is then described as:

$$\tau_v(x) = \tau_{max}(v)x^a \quad (3)$$

where x is the spatial dimension across our LOS and a is the power law index. Then, given two or more intensity profiles, we can solve for τ_{max} and a simultaneously.

The unsaturated absorption troughs of Fe II cover a velocity range $-820 \lesssim v \lesssim -600$ km s $^{-1}$ and have been modeled by a Gaussian profile, based on the Fe II* 1278 Å trough. The corresponding best-fit profile is scaled to match the other Fe II troughs with the final fits shown in Fig. 4. Except for the 7955 and 8680 cm $^{-1}$ levels, all other troughs appear unsaturated and therefore their AOD column densities have been taken as measurements. We also detect multiple unsaturated transitions from the 385, 668, 863 and 1873 cm $^{-1}$ levels and can therefore apply the Power Law (PL) model to obtain their column densities. We find that for these transitions, the N_{ion} values derived from the PL method are similar to the AOD model and therefore lend credibility to the AOD column densities derived for other species. We repeat this analysis for the other observed troughs in the spectrum and report their column densities in Table 1. The reported error bars for the column density measurements include a 20% relative error added in quadrature to account for systemic uncertainties, following the methodology described by Xu et al. (2018).

3.3. Oscillator strength calculation for Fe II transitions

As mentioned earlier, a special feature of the VLT spectrum of J0932+0840 is the detection of unsaturated troughs corresponding to transitions with very small oscillator strengths. The Fe II 1901.78 ground state transition is the weakest such transition with a theoretically determined oscillator strength of 6.25×10^{-5} (Kurucz & Bell 1995), and is thus rarely observed, with the only other detection in a quasar spectra reported by Byun et al. (2024a). This rarity however means that the oscillator strength value for the transition remains poorly constrained by observations, and is prone to uncertainties. As this transition is of central importance in our work (see section 4), we perform our own calculations to obtain an estimate for the oscillator strength along with its uncertainties.

We modeled the Fe II atomic system and computed gf -values for dipole bound-bound transitions using the computer code AUTOSTRUCTURE (Badnell 2011). AUTOSTRUCTURE solves the Breit–Pauli Schrödinger equation with a scaled Thomas–Fermi–Dirac–Amaldi (TFDA) central-field potential to generate orthonormal atomic orbitals. Configuration Interaction (CI) atomic state functions are built using these orbitals. The scaling factors of the potential for each orbital are generally optimized in a multi-configuration variational procedure minimizing a sum over LS term energies or a weighted average of LS term energies. This optimization can be done on non-relativistic LS

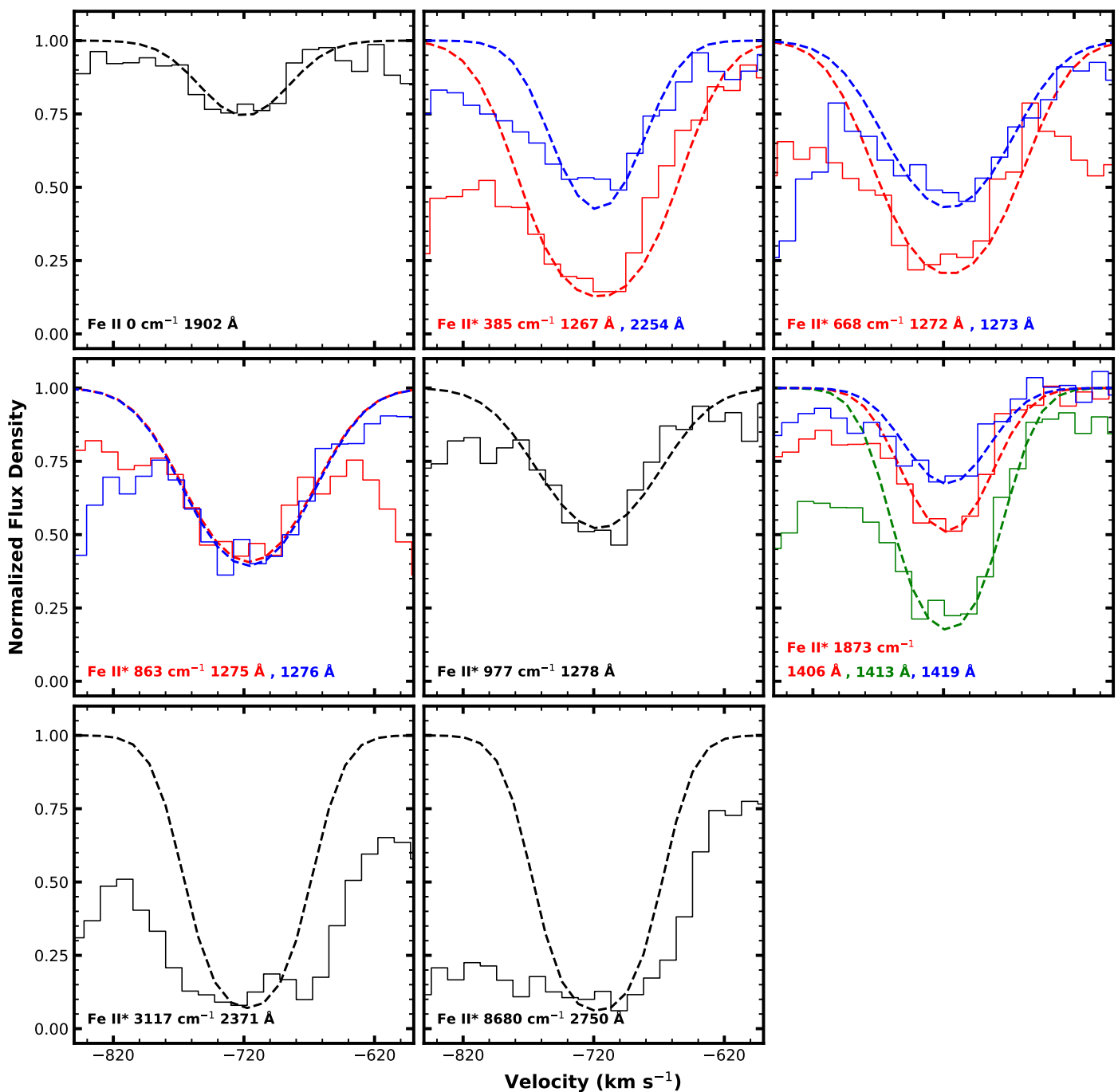


Fig. 4: Identified Fe II troughs for outflow system S2. The histograms show the VLT/UVES spectra in velocity space, and the corresponding dashed curves show the modeled Gaussian for the absorption. The model is based on the 1278 Å transition, and then its template with fixed centroid and width is scaled to match the depth of all other troughs. The lower energy level of the transition and the wavelengths are given for each panel.

calculations or with the inclusion of one-body relativistic operators.

Two types of corrections are enabled by the code after optimizing the orbitals. Perturbative Term Energy Correction (TEC) can be applied to the multi-electronic Hamiltonian, which adjusts theoretical LS term energies closer the centers of gravity of the available experimental multiplets. Also, Level Energy Corrections (LEC) can be applied to shift the theoretical energy levels to reproduce match level energy separations when computing f -values and transitions probabilities.

For large calculations like the present one, AUTOSTRUCTURE is run from our own PYTHON wrapper for semi-automatic generation of input files with large configuration expansions, analysis of output files, and comparisons of energies and radiative data, and TEC and LEC corrections. We carry out numerous calculations for the Fe II system, systematically adding additional configurations to the CI expansion and fully optimizing the orbitals with every expansion. In doing so, we aim at including, within computational limits, all configurations that contribute to improving the energies of the terms belonging to the $3d^64s$, $3d^7$, $3d^54s^2$, $3d^64p$ and $3d^54s4p$ configurations relative to the exper-

Table 1: Absorption lines identified in the VLT spectrum of SDSS J0932+0840 and their measured column densities.

Ion	λ^a (Å)	$\log(f)^b$	E_{low}^c (cm ⁻¹)	N_{ion}^d (log(cm ⁻²))
H I	1215.67	-0.38	0	> 14.57 _{-0.23}
He I*	2829.91	-2.22	159856	14.14 ^{+0.09} _{-0.11}
C II	1334.53	-0.89	0	> 15.20 _{-0.18}
C II*	1335.71	-0.94	63	> 15.24 _{-0.32}
N V	1238.82, 1242.80	-0.80, -1.10	0	> 15.31 _{-0.33}
Mg II	2796.35, 2803.53	-0.22, -0.52	0	> 14.52 _{-0.29}
Al III	1854.72, 1862.79	-0.25, -0.55	0	> 14.70 _{-0.16}
Si II	1808.01	-2.60	0	16.57 ^{+0.11} _{-0.15}
Si II*	1816.93	-2.71	287	16.55 ^{+0.09} _{-0.11}
Si IV	1393.75, 1402.77	-0.29, -0.59	0	> 14.84 _{-0.32}
S II	1250.58, 1253.81	-0.22, -1.92	0	> 16.44 _{-0.31}
Cr II	2056.25, 2062.24, 2066.16	-0.99, -1.12, -1.29	0	> 15.08 _{-0.10}
Cr II*	2161.38	-1.84*	42898	14.95 ^{+0.09} _{-0.11}
Mn II	2576.88	-0.45	0	> 14.04 _{-0.11}
Fe II	1901.78	-4.10 ^{+0.30} _{-0.30}	0 (0)	16.77 ^{+0.36} _{-0.36}
Fe II*	1267.42, 2253.82	-1.85, -2.47	385 (1)	15.50 ^{+0.08} _{-0.10}
Fe II*	1271.98, 1272.61	-1.85, -2.36	668 (2)	15.77 ^{+0.08} _{-0.10}
Fe II*	1275.14, 1275.78	-2.15, -2.00	863 (3)	15.59 ^{+0.08} _{-0.10}
Fe II*	1277.66	-1.85	977 (4)	15.15 ^{+0.08} _{-0.10}
Fe II*	1405.60, 1412.83, 1418.85	-2.92, -2.47, -3.04*	1873 (5)	16.06 ^{+0.09} _{-0.11}
Fe II*	2371.22	-1.84	3117 (8)	> 15.33 _{-0.11}
Fe II*	2749.99	-0.86	8680 (11)	> 14.32 _{-0.10}
Fe III*	1895.48, 1914.07, 1926.32	-0.33, -0.49, -0.60	30089	13.18 ^{+0.13} _{-0.11}
Co II	1941.28, 2012.17	-1.47, -1.43	0	13.94 ^{+0.08} _{-0.10}
Co II*	2286.86	-0.51	3350	14.05 ^{+0.08} _{-0.10}
Ni II	1751.91	-1.54	0	> 15.35 _{-0.21}
Ni II*	2131.93	-2.58*	8394	15.53 ^{+0.09} _{-0.11}
Ni II*	2207.41, 2265.16	-0.79, -0.83	10115	13.59 ^{+0.12} _{-0.17}
Zn II	2026.14	-0.30	0	13.87 ^{+0.08} _{-0.10}

Notes. (a) Rest wavelength of the transition in vacuum. Multiple values, wherever mentioned, correspond to detection of multiple troughs for the given energy level of the ionic species. (b) Logarithm of the oscillator strength of the transition. These were taken from the National Institute of Standards and Technology (NIST) Atomic Spectra Database vers. 5.11, unless marked otherwise. The values marked with an asterisk(*) were obtained from Kurucz & Bell (1995) and the value for the Fe II 1902 transition was determined from our calculations described in section 3.3. (c) Lower energy level of the transition. For Fe II, the indexes used for the energy levels in the CLOUDY modeling are shown in parenthesis. (d) Column density of the ionic transition. Measurements were obtained for unsaturated troughs, whereas saturated troughs only lead to lower limits on the column density of the transition.

imental values, as well as the convergence of the gf-values for the transitions of interest. Particularly challenging and important are the energies of the 3d⁷ a⁴F levels relative to levels the 3d⁶4s a⁶D ground term, from which all observed transitions in this work arise.

Our final expansion includes 11 orbitals (1s, 2s, 2p 3s, 3p, 3d, 4s, 4p, 4d, 5s, 5p) in 61 configurations with 1s and 2s closed core orbitals: 3d⁷, 3d⁶nl ($n = 4 - 5, l = 0 - 2$), 3d⁵nl n' l' ($n = 4 - 5, l = 0 - 2, n' = 4 - 5, l' = 0 - 2$), 3p⁵3d⁸, 3p⁵3d⁷nl ($n = 4 - 5, l = 0 - 2$), 3p⁵3d⁶4s n l ($n = 4 - 5, l = 0 - 2$), 3p⁴3d⁹, 3p⁴3d⁸nl ($n = 4 - 5, l = 0 - 2$), 3p⁴3d⁷nl² ($n = 4 - 5, l = 0 - 2$), 3s3p⁶3d⁸, 3s3p⁶3d⁷nl ($n =$

4 - 5, $l = 0 - 2$), 3s3p⁶3d⁶4s², 2p⁵3s²3p⁶3d⁸, 2p⁵3s²3p⁶3d⁷nl ($n = 4 - 5, l = 0 - 2$), 2p⁵3s²3p⁶3d⁶4s², 2p⁶3p⁶3d⁹, 2p⁶3p⁶3d⁸4s, 2p⁶3p⁶3d⁷4s², 2p⁶3p⁶3d⁷4s4p, 2p⁴3s²3p⁶3d⁹, 2p⁴3s²3p⁶3d⁸4s, 2p⁴3s²3p⁶3d⁷4l² ($l = 0 - 2$).

An important issue to highlight with these calculations is that once an acceptable level of converse was achieved in terms of the predicted energies, further slight optimization of the 3d and 4s orbitals had to be done manually on fine structure energy levels rather than the numerical optimization based on LS terms incorporated in AUTOSTRUCTURE. This is to get the right ordering and energy separations between the 3d⁷ a⁴F and 3d⁶4s a⁶D lev-

els. The reason being that the energy separation between these is comparable to the magnitude of the two-body relativistic corrections, hence optimizations in LS-coupling of these terms turns out to be unphysical and become severely disrupted in final jj-coupling computations. Moreover, the relativistic jj-coupling correction on level energies are highly non-linear upon initial LS terms energies. Also due to the magnitude of 2-body energy corrections on levels of the $3d^7 a^4F$ and $3d^6 4s a^6D$ no perturbative TEC can be employed. Rather, the orbitals must be optimized by hand up to obtaining accurate level energies, then simple LEC are applied for the final computation of gf -values.

Our calculation results into 669 energy levels from the five configurations listed above. These levels yield nearly 40,000 dipole allowed transitions and over 100,000 dipole forbidden transitions. This extensive dataset enables proper identification of the troughs observed in our experiment, many of which were not found in previously published tabulations of Fe II gf -values. Regarding the Fe II troughs identified in the VLT/X-Shooter spectrum of J0932+0840, it should be borne in mind these are intrinsically weak transitions, hence their gf -values carry significant uncertainty. The radiative rates found for these transitions in the NIST database have accuracy ratings of “D” or “D+” (i.e., uncertainty $\gtrsim 50\%$). Table 2 compares the gf -values from the NIST database with our present calculations for a sample of transitions.

For the transitions that have an available gf -value in the NIST database, we use that value in our analysis. For the Fe II 1901.78 Å transition, we use the value obtained from our calculations, with $\log(gf) = -3.1^{+0.3}_{-0.3}$. This is in agreement with the value reported in Kurucz & Bell (1995). Our calculations importantly also give us an estimate for the associated uncertainty, which we propagate in our calculation for the Fe II ground state column density (Table. 1) and thus the rest of our analysis.

3.4. Photoionization modeling

Photoionization dominates the ionization equilibrium in quasar outflows. Therefore an outflow is characterized by its total hydrogen column density (N_H) and ionization parameter (U_H), which is related to the rate of ionizing photons emitted by the source (Q_H) by:

$$U_H = \frac{Q_H}{4\pi R^2 n_H c} \quad (4)$$

where R is the distance between the emission source and the observed outflow component, c is the speed of light, and n_H is the hydrogen number density. Q_H is determined by the choice of the spectral emission distribution (SED) that is incident upon the outflow and the redshift of the object.

Using the obtained column densities, we can constrain N_H and U_H , thus determining the physical state of the gas. This is done using version C23.01 of the spectral synthesis code CLOUDY (Chatzikos et al. 2023), which solves the ionization equilibrium equations. The outflow is modeled as a plane parallel slab with a constant n_H ($= 10^5 \text{ cm}^{-3}$, see section 4.2) and solar abundance, and is irradiated upon by the modeled SED from the quasar HE0238-1904 (Arav et al. 2013), which is the best empirically determined SED in the extreme UV where most of the ionizing photons come from. Using the methodology described by Arav et al. (2001b) and Edmonds et al. (2011), N_H and U_H are varied in small steps keeping all other parameters constant. This leads to a grid of models in the (N_H, U_H) parameter space, with each point in the grid predicting the total column densities (i.e., the

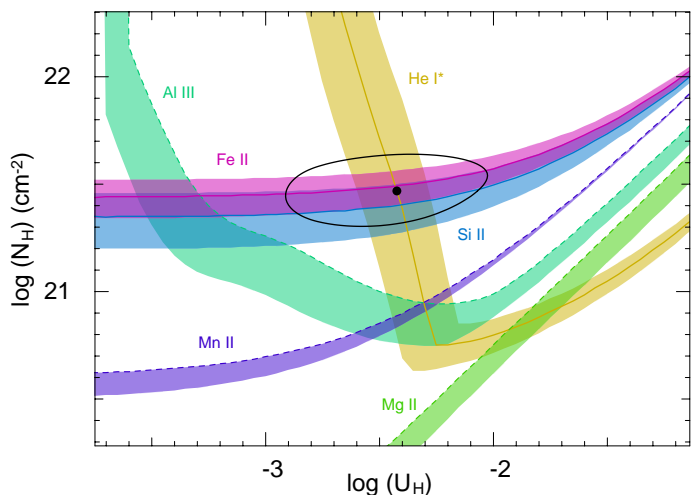


Fig. 5: Plot of Hydrogen column density ($\log N_H$) vs. ionization parameter ($\log U_H$), with constraints based on the measured total ionic column densities (sum of the column densities of the ground state and all the observed excited states). Measurements are shown as solid curves, while the dashed curves show lower limits. The shaded regions denote the errors associated with each N_{ion} . The phase space solution with minimized χ^2 is shown as a black dot surrounded by a black eclipse indicating the 1- σ error.

sum of the column densities of the ground state and all the excited states) of all relevant ions. We then map the measured ionic column densities (N_{ion}) against the model predictions, resulting in a phase space plot containing the ionic equilibrium solutions for all observed ions as shown in Fig. 5. In this space an (N_H, U_H) value that is within one standard deviation of all the solutions would provide a viable model. The best-fit solution determined by minimizing χ^2 leads to $\log N_H = 21.47^{+0.17}_{-0.16} [\text{cm}^{-2}]$ and $\log U_H = -2.4^{+0.4}_{-0.5}$. We note that this solution does not depend strongly on the assumed value of n_H in the range considered in this work ($3 \lesssim \log(n_H) \lesssim 8 [\text{cm}^{-3}]$), as verified by CLOUDY models.

While we have robust column density measurements from multiple troughs corresponding to Co II and a single trough corresponding to Zn II, we do not use them to constrain our photoionization solution. This is because the ionization structure of the singly ionized iron-peak elements is very similar to that of Fe II. Therefore their contours in the (N_H, U_H) phase space shown in Fig. 5 are parallel to that of Fe II, with the exact location dependent on their respective abundances. As Co and Zn are much less abundant than Fe, their ionization structure is more prone to be affected by slight variation in their abundances as compared to Fe, and therefore we do not include them in our determination of the best-fit photoionization solution.

4. Number density of the outflow

4.1. Electron number density

In the absorption system S2 of the outflow in J0932-0840, we have detected multiple troughs arising from excited metastable levels of Fe II (see Fig. 4). Under the assumption of collisional excitation, the ratios of the column densities of these excited lines to the resonance line can be used as an indicator of the electron number density (n_e) of the outflow (e.g., de Kool et al. 2001; Arav et al. 2018). To do so, we obtain the theoretical population ratios between the various excited states and the ground

Table 2: Comparison between the gf values obtained from our calculations and the values available in the NIST database for a sample of transitions.

Transition	Wavelength (Å)	log(gf)	
		NIST	This work
$3d^6 4s \text{ a } ^6D_{7/2} - 3d^5 4s 4p \text{ x } ^6P_{5/2}^o$	1267.43	-0.95	-0.70
$3d^6 4s \text{ a } ^6D_{5/2} - 3d^5 4s 4p \text{ y } ^6P_{5/2}^o$	1271.99	-1.08	-0.82
$3d^6 4s \text{ a } ^6D_{5/2} - 3d^5 4s 4p \text{ y } ^6P_{3/2}^o$	1272.62	-1.58	-1.11
$3d^6 4s \text{ a } ^6D_{3/2} - 3d^5 4s 4p \text{ y } ^6P_{5/2}^o$	1275.15	-1.60	-1.29
$3d^6 4s \text{ a } ^6D_{3/2} - 3d^5 4s 4p \text{ y } ^6P_{3/2}^o$	1275.78	-1.40	-0.92
$3d^6 4s \text{ a } ^6D_{1/2} - 3d^5 4s 4p \text{ y } ^6P_{3/2}^o$	1277.65	-1.54	-1.06
$3d^7 \text{ a } ^4F_{9/2} - 3d^6 4p \text{ z } ^2F_{7/2}^o$	1405.61	-1.90	-2.32
$3d^7 \text{ a } ^4F_{9/2} - 3d^6 4p \text{ z } ^4D_{7/2}^o$	1412.84	-1.47	-1.30

state as a function of n_e using the CHIANTI atomic database (vers. 9.0 Dere et al. 1997, 2019). We then compare these predictions with our measurements of the column density ratios with the results shown in Fig. 6. The various excited levels constrain $\log(n_e)$ to be between 3.1 and 3.75 [cm^{-3}]. We determine its weighted mean using the methodology described by Barlow (2004), and obtain the error using the procedure described in Appendix A. This results in $\log(n_e) = 3.42^{+0.65}_{-0.46}$.

In determining n_e , we used $T_e = 5000$ K, based on the average Fe II temperature determined from our photoionization modeling. This temperature is lower than the common assumption of $T_e \approx 10,000$ K for photoionized outflows. However, it does not significantly affect our solution for n_e as its dependence on the temperature in this range is weak. This can be understood by noting that for a given energy level, the relative excited state population depends on temperature through the Boltzmann factor $e^{-\Delta E/kT}$, where ΔE is the energy of the transition and k is the Boltzmann constant. For the Fe II* levels used in determining n_e , $\Delta E \leq 1873 \text{ cm}^{-1}$ and thus, $\Delta E/k \lesssim 2700$ K. Therefore, for higher temperatures, the contribution from the Boltzmann factor does not vary significantly, and the dependence of the relative excited state population on the temperature is thus weak.

We have also measured the column densities of troughs corresponding to two excited metastable levels of Ni II (and a lower limit for the ground state). However, as Dunn et al. (2010) have noted, Ni II cannot be used as a reliable indicator of the outflow's electron number density. This is because as opposed to Fe II, Ni II is much more prone to fluorescence excitation by the UV continuum (Lucy 1995; Bautista et al. 1996). Therefore the population of the Ni II excited levels is highly sensitive to the incident radiation, thus making it hard to model its excited state population. We thus focus solely on Fe II for our density diagnostics.

4.2. Hydrogen number density

We can perform a similar analysis for the hydrogen number density (n_H) by modeling the photoionized gas using CLOUDY, which offers two advantages over the CHIANTI analysis. First, CLOUDY does not assume fixed values in electron density (n_e) and temperature (T_e) within the gas. Instead, for a given value of the gas density n_H and a choice of elemental abundances, n_e , T_e , and the ion number densities are computed self-consistently, given the depth-dependent thermal and ionization equilibrium solutions determined zone-by-zone through the cloud. Secondly, since an assumption about the outflow's gas density n_H is part of

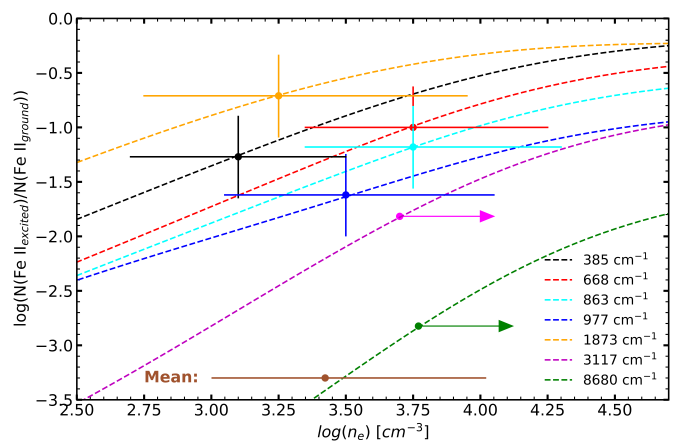


Fig. 6: Dashed curves represent the theoretical population ratios for different Fe II* transitions for an effective electron temperature $T_e = 5000$ K (determined from our CLOUDY modeling). The solid crosses represent the observed column density ratios and their corresponding error (which includes the error determined in section 3.3). The arrows represent the lower limits obtained from possibly saturated troughs corresponding to these energy levels. The mean n_e along with its errors obtained from all the levels is shown in brown.

the ionization equilibrium solution, there is no need to guess its value based upon the value of the electron density n_e determined from the level-population/excitation analysis. The CLOUDY models also include the contributions from fluorescence excitation (and other microphysics) in addition to collisional excitation, although this is not expected to significantly affect the relevant Fe II level populations, as mentioned in the previous section.

For our analysis, we run models for the outflow with fixed N_H and U_H (obtained from our photoionization modeling in section 3.4), for a range of n_H ($10^{4.0} \leq n_H [\text{cm}^{-3}] \leq 10^{6.5}$, in steps of 0.5 dex). These models predict the column densities for all the available levels of Fe II, from which we can obtain the column density ratios for the various levels to the ground state and compare them with the ratios obtained from the spectrum. The results of this analysis are shown in Fig. 7.

The different excited state ratios are reproduced for hydrogen number densities between $4.5 \leq \log(n_H) \leq 5.0$ [cm^{-3}]. To find the best-fit value of n_H from this analysis we vary $\log(n_H)$

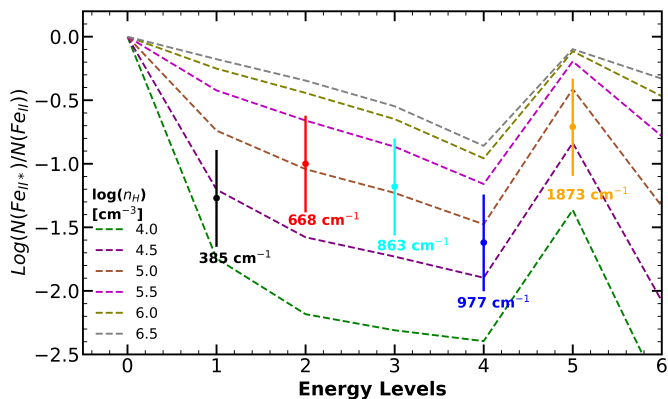


Fig. 7: Excited state to ground state ratios for Fe II: The dashed lines show the level population ratio predicted by CLOUDY for different values of hydrogen number density. The measurements are shown as coloured circles, and are accompanied by their errors.

between 4.0 and 5.5 [cm^{-3}], in steps of 0.1 to create a grid of models. We then compare the observed column density ratios of the excited states with the model predictions to perform a χ^2 minimization. This results in a best-fit solution with $\log(n_H) = 4.8$ [cm^{-3}]. We discuss the relation between the electron number density solution determined using CHIANTI ($\log(n_e) = 3.42$ [cm^{-3}]) and the hydrogen number density solution determined from CLOUDY ($\log(n_H) = 4.8$ [cm^{-3}]) in the next section.

4.3. Physical structure of the cloud

We can better understand the formation of Fe II and the excitation of various energy levels by taking a detailed look at the physical structure of the photoionized cloud. As found through the photoionization modeling in Fig. 5, the cloud is bound by a total hydrogen column density of $\log(N_H) = 21.47$ [cm^{-2}]. Using $\log U_H = -2.4$ and the HE0238 SED, we employ CLOUDY to provide a zone-wise description of the cloud for the best-fit hydrogen number density solution obtained in 4.2 ($\log(n_H) = 4.8$ [cm^{-3}]). Fig. 8 shows the obtained physical parameters (electron temperature T_e , and electron number density n_e) and the column densities for the observed Fe II levels, as a function of the hydrogen column density within the cloud. We define the hydrogen ionization front (marked by the black dashed line) as the point in the cloud where half the hydrogen is ionized, and therefore the density of fully ionized hydrogen (H II) and neutral hydrogen (H I) is similar.

Fig. 8 (top panel: blue curve) shows that the temperature within the cloud drops suddenly across the H I ionization front. This is because most of the highly energetic photons are absorbed at the front. The electron number density also remains fairly constant before the H I front. In this region, as most of the Hydrogen is fully ionized, the electron number density is linearly related to the hydrogen number density with $n_e \approx 1.2 n_H$ (approximation for fully ionized plasma; Osterbrock & Ferland 2006). However, across the H I front, n_e drops suddenly by around an order of magnitude as seen in Fig. 8 (top panel: red curve). This decrease is attributed to hydrogen becoming neutral and thus absorbing most of the free electrons. The bottom panel shows that the column densities of all observed levels of Fe II also vary rapidly near the front, with a sudden increase occurring just inside. The hydrogen ionization front is essential for

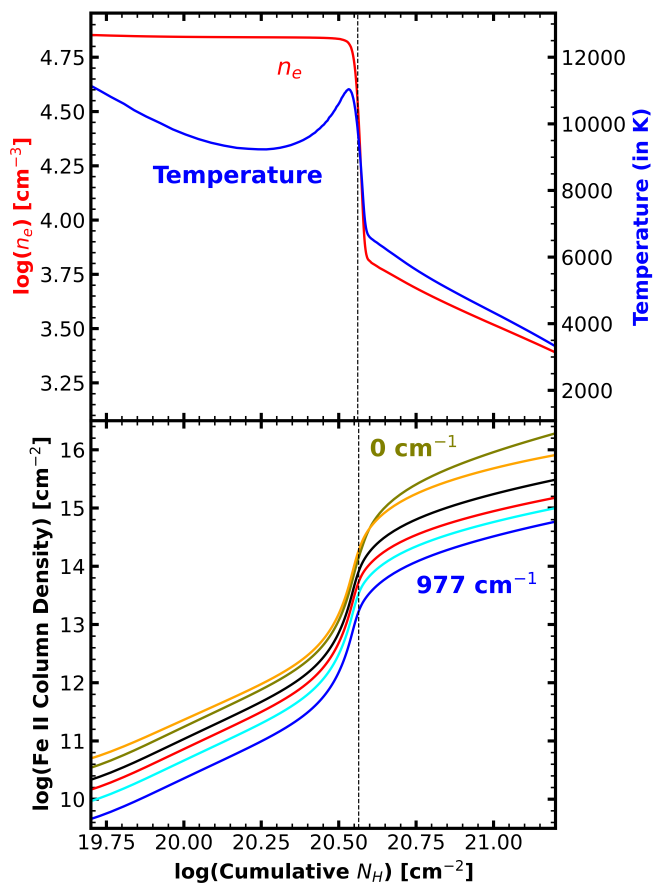


Fig. 8: Physical structure of the photo-ionized cloud vs the total hydrogen column density for $\log(n_H) = 4.8$ [cm^{-3}]. The top panels show how the electron density and temperature vary within the cloud. The bottom panels show the cumulative column density of each Fe II level detected in the spectra. The dashed black vertical line marks the H I ionization front.

effective formation of Fe II as it acts as a shield against high energy photons, thus preventing its further ionization. Therefore, most of the observed Fe II comes from the region of the cloud beyond the H I front. The varying electron number densities and temperatures in this region indicate that the conditions that determine the collisional excitation equilibrium are starkly different before and after the H I ionization front. This is an important effect, as it shows that the majority of Fe II is subjected to a significantly reduced electron number density than the rest of the cloud, where it traces the constant hydrogen number density. Therefore, in FeLoBAL outflows, the approximation $n_e \approx 1.2 n_H$ is not correct, and using this approximation can lead to a severe underestimation for n_H .

We can estimate the effective T_e and n_e for Fe II by averaging over all the zones while weighing their contribution based on their relative Fe II populations. This results in $T_{e,eff} = 5060$ K and $\log(n_{e,eff}) = 3.51$ [cm^{-3}]. This is in remarkable agreement with the solution obtained from CHIANTI in section 4.1 with $\log(n_e) = 3.42^{+0.60}_{-0.42}$ [cm^{-3}]. This shows that the two solutions obtained independently for n_e and n_H , respectively, are consistent with each other and we thus adopt $\log(n_H) = 4.80^{+0.60}_{-0.52}$ [cm^{-3}] for the cloud.

We note that this is not the first time a difference between the two density solutions has been deduced for a low-ionization

quasar outflow. [Dunn et al. \(2010\)](#) found n_H for their outflow to be ~ 0.4 dex higher than n_e . Similarly, [de Kool et al. \(2001\)](#) found that their models required n_H to be $\sim 0.4/1.4$ dex higher than n_e depending on the choice of abundance and depletion model. On the other hand, [Moe et al. \(2009\)](#) and [Bautista et al. \(2010\)](#) have shown that for their models, $n_e \approx n_H$. These different studies have thus revealed that the low-ionization gas in such outflows is subject to a diverse range of physical conditions.

5. Distance and Energetics

5.1. Distance to the outflow

Having obtained U_H from photoionization modeling (section 3.4) and n_H (section 4), we can invert eqn. (4) to obtain the distance of the outflow from the emission source (R) as:

$$R = \sqrt{\frac{Q_H}{4\pi U_H n_H c}} \quad (5)$$

To obtain the rate of hydrogen ionizing photons emitted by the source (Q_H), we scale the HE0238 SED used in our modeling to match the estimated SDSS flux of J0932+0840 at an observed wavelength of $\lambda \approx 5680 \text{ \AA}$, with $F_\lambda = 7.35 \times 10^{-17} \text{ erg s}^{-1} \text{ cm}^{-2} \text{ \AA}^{-1}$. Integrating over the scaled SED for energy values above 1 Ryd. gives us $Q_H = 4.52^{+0.45}_{-0.45} \times 10^{56} \text{ s}^{-1}$ and Bolometric Luminosity $L_{Bol} = 8.10^{+0.81}_{-0.81} \times 10^{46} \text{ erg s}^{-1}$. This results in the location of the outflow being $0.7^{+0.9}_{-0.4}$ kpc away from the central source.

5.2. Black hole mass and Eddington luminosity

As described in section 2.2, $\text{Mg II } 2799 \text{ \AA}$ is one of the most prominent emission features in the SDSS spectra. Based on the scaling relation derived in [Bahk et al. \(2019\)](#), we can estimate the black hole mass (M_{BH}) from the Mg II emission line as:

$$\log\left(\frac{M_{BH}}{M_\odot}\right) \approx (6.79 \pm 0.06) + 0.5 (\log L_{3000,44}) + 2 \log(\text{FWHM}_{\text{Mg II}}) \quad (6)$$

where $L_{3000,44}$ is the rest frame luminosity λL_λ at 3000 \AA in units of $10^{44} \text{ erg s}^{-1}$, and $\text{FWHM}_{\text{Mg II}}$ is in units of 1000 km s^{-1} . Based on our modeling in Fig. 2, $\text{FWHM}_{\text{Mg II}} \approx 3430 \text{ km s}^{-1}$, and from our continuum modeling of the SDSS spectrum at 3000 \AA , $\lambda L_\lambda = 2.86^{+0.43}_{-0.43} \times 10^{46} \text{ erg s}^{-1}$. Using these values with eqn. (6) leads to $\log(\frac{M_{BH}}{M_\odot}) = 9.09^{+0.1}_{-0.1}$, which results in Eddington Luminosity $L_{edd} = 1.54^{+0.36}_{-0.30} \times 10^{47} \text{ erg s}^{-1}$.

5.3. Energetics

Assuming a simple geometry for the outflow in the form of a partial spherical shell covering fractional solid angle Ω , and moving with velocity v , the total mass is (see [Borguet et al. \(2012\)](#) for a detailed discussion):

$$M \approx 4\pi\Omega R^2 N_H \mu m_p \quad (7)$$

where R is the distance of the outflow from the source, N_H is the outflow's total hydrogen column density, m_p is the proton mass, and $\mu = 1.4$ is the atomic weight of the plasma per proton.

Table 3: Physical parameters of quasar J0932+0840 and its outflow S2.

v (km s ⁻¹)	-720
$\log N_H$ [cm ⁻²]	$21.47^{+0.17}_{-0.16}$
$\log U_H$	$-2.4^{+0.4}_{-0.5}$
$\log n_H$ [cm ⁻³]	$4.80^{+0.60}_{-0.52}$
R (kpc)	$0.7^{+0.9}_{-0.4}$
\dot{M} ($M_\odot \text{ yr}^{-1}$)	43^{+65}_{-26}
$\log \dot{E}_k$ [erg s ⁻¹]	$42.85^{+0.40}_{-0.39}$
L_{Edd} (erg s ⁻¹)	$1.54^{+0.36}_{-0.30} \times 10^{47}$
L_{Bol} (erg s ⁻¹)	$8.10^{+0.81}_{-0.81} \times 10^{46}$
\dot{E}_k/L_{Edd}	$0.5^{+0.7}_{-0.3} \times 10^{-4}$
\dot{E}_k/L_{Bol}	$0.9^{+1.3}_{-0.5} \times 10^{-4}$

Defining the dynamic time scale $t_{dyn} = R/v$, where v is the outflow velocity, the mass flow rate \dot{M} and the kinetic luminosity \dot{E}_k can be obtained:

$$\dot{M} = \frac{M}{t_{dyn}} = 4\pi\Omega R N_H \mu m_p v \quad (8)$$

$$\dot{E}_k = \frac{1}{2} \dot{M} v^2$$

As Ω cannot be determined from the spectrum, the fraction of quasars that show the particular class of outflows has been commonly used as a substitute. Although FeLoBALs are extremely rare as detailed in the introduction, we use $\Omega \approx 0.2$, based on the fraction of quasars that show C IV BALs (which is seen in the SDSS spectra of J0932+0840). This is due to the argument put forth by [Dunn et al. \(2010\)](#) based on the morphological indistinguishability of the C IV BALs in FeLoBALs with C IV BALs in the ubiquitous high ionization BALQSOs. Based on this, FeLoBALs fall under the class of normal $\Omega \approx 0.2$ outflows that we are seeing through a rare LOS.

This results in a mass loss rate of $\dot{M} = 43^{+65}_{-26} M_\odot \text{ yr}^{-1}$ and kinetic luminosity $\dot{E}_k = 0.7^{+1.1}_{-0.4} \times 10^{43} \text{ erg s}^{-1}$, which is $0.5^{+0.7}_{-0.3} \times 10^{-4}$ of the quasar's L_{Edd} and $0.9^{+1.3}_{-0.5} \times 10^{-4}$ of its L_{Bol} . (See Table 3 for a summary of the obtained parameters for the quasar and its outflow.) [Hopkins & Elvis \(2010\)](#) show that a kinetic luminosity of $\sim 5 \times 10^{-3}$ of the quasar's luminosity is required for efficient AGN feedback. As the kinetic luminosity of this outflow component is much less than this requirement, it is not expected to contribute significantly towards AGN feedback processes.

6. Discussion

6.1. Variability of the broad absorption lines

As mentioned in section 2, we have two different epochs of SDSS spectra that were obtained ~ 8 years apart, which spans roughly $8/(1+z) \sim 2.4$ yrs in the rest frame of the quasar. We compare them over their common wavelength range ($4000 - 9000 \text{ \AA}$ in the observed frame) and find that there is no discernible change in the continuum as the flux level remains the

same in regions with no emission/absorption. The outflow identified in the UVES spectrum can also be seen clearly in the SDSS spectra. However, due to its lower resolution, the three narrow low velocity components ($v \sim -500, -700$ and -850 km s^{-1}) appear as a single component, whereas, the broader high velocity components ($v \sim -1300, -4200$ and -5000 km s^{-1}) are well resolved. The low velocity component does not vary significantly over the two epochs for any of the observed ionic species. This is best confirmed by looking at the non-black troughs corresponding to the low ionization species (e.g., Si II, Fe II and Ni II). For the high ionization species (e.g. C IV, Si IV and N V), as their troughs are completely saturated, discerning any variation is harder and thus it cannot be completely ruled out.

For the broad high velocity components, however, a clear change can be seen, as most of the non-black troughs become considerably shallower. Fig. 9 shows this phenomenon for Al III which shows the most dramatic decrease among all observed species. The low velocity components for Al III, Si II and Si II* (marked with black vertical lines) do not show any appreciable variation. However, the high velocity Al III component (between $6010 < \lambda_{obs} < 6080 \text{ \AA}$) shows stronger absorption and a more pronounced kinematic structure for the 2003 spectrum as compared to the 2012 spectrum. Possible explanations for this variation in the high velocity structure include: (i) transverse motion of the outflowing gas across our line of sight, or (ii) a change in the ionization state of the gas. In section 6.1.1 and 6.1.2, we consider both these scenarios.

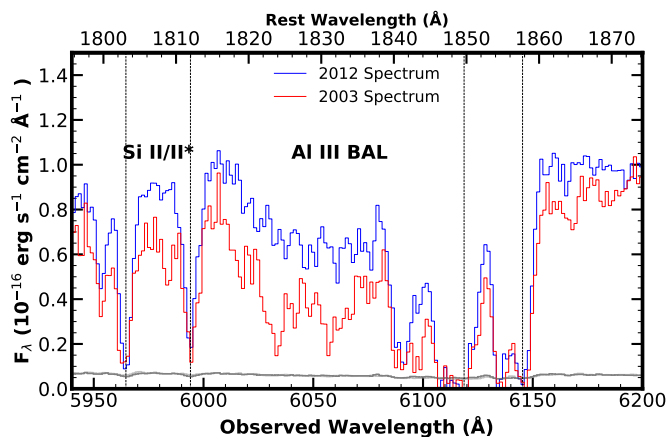


Fig. 9: Spectral region around the Al III BAL as observed in the 2003 (in red) and 2012 spectra (in blue). Troughs corresponding to our main outflow system at $v \approx -700 \text{ km s}^{-1}$ are marked with a black dashed line. We choose this spectral region as it shows the most noticeable difference in the high velocity structure between the two epochs.

6.1.1. Transverse motion

In this case, variability in the troughs is assumed to be due to the transverse motion of the absorbing gas such that its coverage of the continuum source along our line of sight changes. With the help of some simplifying assumptions, we can determine the transverse velocity of the variable component and an upper limit for its distance from the central source following previous studies. (e.g., Moe et al. 2009; Hall et al. 2011; Yi et al. 2019). Assuming that the black hole is accreting close to the Eddington limit, we can use its Bolometric luminosity (L_{bol}) and black-hole

mass (M_{BH}) to estimate the radius of the accretion disk. Using eqn. (3.15) of Peterson (1997) and the accretion disk size-black hole mass relation derived by Morgan et al. (2010), we find the accretion disk radius to be of the order of a light day.

The residual intensity of the Al III component shown in Fig. 9 increases by ~ 0.4 in 2.4 yrs in the quasar rest frame. In the simplest scenario, this would imply that the transverse motion of the gas allowed it to cross roughly 40% of the 2 light-day wide continuum source in the span of 2.4 yrs. This results in a lower limit for the transverse velocity with $v_{tr} \gtrsim 275 \text{ km s}^{-1}$. Finally, if we assume that this tangential velocity is not larger than the Keplerian orbital velocity solely due to the supermassive black hole (SMBH), we can obtain an upper limit on the distance of the high velocity component from the center as $R < GM_{BH}/v^2 \approx 70 \text{ pc}$.

However, at such large distances, the outflowing gas could be affected by the potential of the stars in the galactic bulge. We can check whether this contribution is significant by obtaining the radius of influence (r_h) of the SMBH. r_h is defined as the radius where the Keplerian rotation velocity equals the velocity dispersion of the galaxy, and is thus a typical estimate of the radius within which the SMBH must dominate the gravitational potential (Peebles 1972). Using eqn. (17.1) and (17.6) of Bovy (in prep.)¹, we obtain $r_h \approx 46 \text{ pc}$. As this is smaller than our upper limit on the distance (70 pc), we need to include the contribution from the galactic bulge. Within the sphere of influence, the total mass of the stars is roughly equal to that of the SMBH. If we assume that density of the galactic bulge is roughly constant around the center (within the scale of a few hundreds of parsecs), we can obtain the enclosed stellar mass as a function of the radius, with $M_*(< r) \approx M_{BH} (r/r_h)^3$. Then, we can solve for the Keplerian velocity profile as:

$$v(r) \approx \sqrt{G \left(\frac{M_{BH} + M_*(< r)}{r} \right)} \quad (9)$$

This reveals that the Keplerian velocity decreases as we move away from the center, as the mass of stars initially is much less compared to that of the SMBH. However, as we keep moving away, more and more stellar mass is accumulated and eventually it becomes the dominant factor. Therefore, the velocity eventually stops decreasing, with a minimum at $r \approx 0.8 r_h$, beyond which it increases monotonically as far as the bulge extends. In our case, the minimum Keplerian velocity (v_{min}) $\approx 470 \text{ km s}^{-1}$ is larger than the lower limit on the transverse velocity obtained for the outflowing component. Therefore, we cannot obtain any estimate on its distance based on the available information about the variability.

Finally, we note that while considering the case for transverse motion of the gas, we have assumed that the variable broad structure (with $\Delta v \gtrsim 3000 \text{ km s}^{-1}$) seen in Fig 9 is a single outflow component. If, however, this broad feature is composed of different velocity components that could be at different radii from the central source, the observed variability would require their coordinated movement, which is unlikely. In such a scenario, a change in the ionization state of the gas is a more viable explanation for the variability (see section 5.1 of Capellupo et al. 2013, for a detailed discussion).

¹ An online draft of the work is available at <https://galaxiesbook.org/>.

6.1.2. Change in ionization state

As the ionization equilibrium of the outflow is dominated by photoionization, a change in the incident ionizing flux should lead to a change in the ionization state of the absorbing gas, which would then be reflected in the corresponding troughs. In this section, we consider whether such a mechanism could explain the nature of the absorption trough variability in the SDSS spectra of J0932+0840. Our model focus on three physical and observational constraints: 1. Plausibility of change in the ionizing flux, 2. Lack of variation in the Si II 1808, 1817 Å troughs for our main outflowing system and 3. Significant change in the Al III $\lambda\lambda$ 1855, 1863 doublet corresponding to a higher velocity outflowing system. We now discuss each of these in detail below.

1. For J0932+0840, as the spectra do not cover the wavelength region responsible for the ionizing radiation ($\lambda_{rest} \leq 912$ Å), we do not have direct information about variation in the ionizing flux. For the spectral region covered by the two SDSS epochs ($1200 \leq \lambda_{rest} \leq 2700$ Å), we do not see any appreciable change in the underlying continuum emission, which hints against any drastic changes in the shorter wavelength regime as they are usually assumed to be correlated. However, exception to this correlation has been observed by [Arav et al. \(2015\)](#), and therefore variation in the ionizing flux cannot be ruled out based on the far UV flux alone. To study in detail the effect of any possible variation, we consider an example in which the ionizing flux increases by a factor of ~ 2 between the two epochs.

2. We first consider the main outflowing component at $v \sim -700$ km s⁻¹, for which no significant variation was detected in the non-black troughs from the low-ionization species (e.g., see the Si II troughs in Fig. 9). To study the maximum variation in the ionization state of the gas as a result of the increase in ionizing flux, we assume that a new ionization equilibrium is established over a time scale shorter than the separation between the epochs. Eqn. 4 shows that the new ionization parameter ($U_{H_{2012}}$) should then be related to the old ionization parameter ($U_{H_{2003}}$) as $U_{H_{2012}}/U_{H_{2003}} \sim 2$, while other parameters such as N_H and n_H remain unchanged. If we assume that the ionization parameter of this component during the 2003 epoch is similar to that obtained from the VLT/UVES spectrum, we have $\log(U_{H_{2003}}) = -2.4$ and $\log(U_{H_{2012}}) = -2.1$. We compare our photoionization models (with $\log(N_H) = 21.5$ [cm⁻²]) of the outflowing gas in both these ionization states and find that the Si II column density decreases by only $\sim 10\%$ despite a 100% increase in the ionizing flux. To better understand this phenomenon, we track the decrease in the Si II column density as a function of N_H , with the results shown in Fig. 10. We find that for the same variation in the ionizing flux, the percentage change in Si II column density can be different by up to an order of magnitude, depending on the total hydrogen column density of the cloud.

This effect can be understood by noting that the formation of singly-ionized species like Si II is heavily dependent on the hydrogen ionization front (see section 4.3), which forms around $\log(N_H) \sim 20.5$ [cm⁻²] in our case. Before the H I front, only a small fraction of Silicon is in the form of Si II, with the majority being in the more ionized forms (e.g., Si III/IV). The exact amount of Si II is thus determined by a delicate ionization balance with the higher ionized species which is highly dependent on the incident ionizing flux. Therefore, variations in this flux are reflected strongly in the Si II column density before the H I front. On the other hand, after the front, most of the Silicon is found to be in the form of Si II ($> 90\%$ for $\log(N_H) \geq 21.5$ [cm⁻²]). With the increase in ionizing flux, the H I front shifts to a higher N_H , however, it still continues to shield the gas behind it from Si II

ionizing photons (i.e., photons with energy greater than the ionization potential of Si II ~ 16.35 eV) and the ionization balance of Silicon there continues to be dominated by Si II. Therefore, the Si II column density for the clouds with higher N_H is much less sensitive to the change in the ionizing flux. This is also true for other singly ionized species (e.g. Fe II and Ni II) and thus their column densities are also not expected to vary significantly in the case of our main outflowing component, which is consistent with our observations.

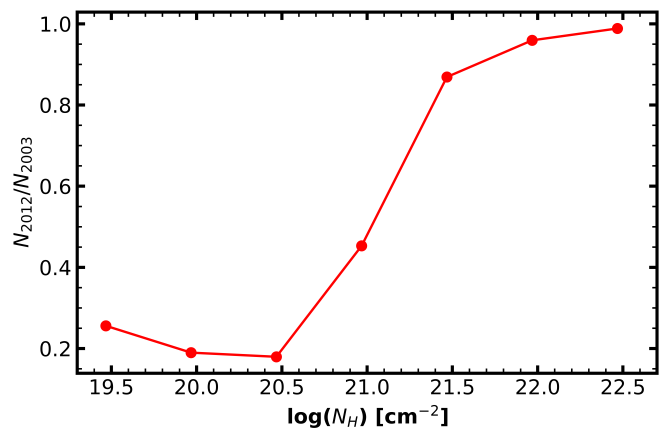


Fig. 10: Change in the column density of Si II due to a factor of 2 increase in the ionizing flux for clouds with different total hydrogen column density (N_H). For clouds that have not formed the H I ionization front ($\log(N_H) \leq 20.5$), the variation in column density is much higher than for the clouds that have formed the ionization front.

3. We now consider the higher velocity component at $v \sim -5100$ km s⁻¹, which shows troughs from multiple species such as Si II, C II, Al III, Mg II, Si IV and C IV. The Al III $\lambda\lambda$ 1855, 1863 doublet for this component is shown in Fig. 9 between 6020-6070 Å, where it shows considerable variation between the two epochs. There are also clear signs of variations for the unsaturated troughs of Si II 1260 Å and C II 1335 Å, however, the troughs corresponding to Mg II, Si IV and C IV are saturated and thus their variation cannot be characterized properly. While the photoionization solution of this component is not well constrained, we consider whether this variation in the low-ionization components could be understood in terms of a change in the ionization state of the gas. [Krolik & Kriss \(1996\)](#) provide an estimate for the recombination timescale (t^*) over which a sudden change in the incident ionizing flux would lead to a change in the ionic fraction of a species. For our main outflowing component, we find $t_{Al III}^* \sim 1.24$ yrs. We do not have a density diagnostic for the high velocity component and thus cannot obtain its recombination timescale directly. However, we note that due to its much higher velocity, this component is expected to be closer to the central source, and thus have a higher hydrogen and electron number density than our main outflowing component (from Eqn. 5). As t^* is inversely proportional to n_e for similar temperatures, we expect the recombination timescale of the high velocity component to be significantly smaller than 1.24 yrs. It would thus be much smaller than the 2.4 yr span between the two epochs in the quasar rest frame. Therefore, the new Al III column density will be in good agreement with that predicted by the time-independent photoionization equilibrium equations.

To study this variation quantitatively, we first obtain the column density of the Al III 1863 Å trough in the 2003 epoch using Eqn. 1. This was done by assuming an AOD model and integrating over the velocity range $-5450 \leq v \leq -4550 \text{ km s}^{-1}$, which results in $\log(N_{\text{Al III}}) = 14.81 \text{ [cm}^{-2}\text{]}$. We repeat this process (with the same velocity range) for the 2012 epoch and find $\log(N_{\text{Al III}}) = 14.49 \text{ [cm}^{-2}\text{]}$. If this decrease in Al III column density is due to a change in the ionization state, we should be able to find a constant value of N_H and the two ionization parameters (U_H and U'_H) that can reproduce the observed Al III column densities for the two epochs. We again assume that the ionizing flux increases by a factor of 2 between the two epochs, and therefore, we have $U_H/U'_H = 0.5$. With this constraint in mind, we explore a (N_H, U_H) phase-space plot (similar to Fig. 5) for the measured Al III column densities and obtain $\log(N_H) = 21.1 \text{ [cm}^{-2}\text{]}$, $\log(U_H) = -2$ and $\log(U'_H) = -1.7$. This variation would also predict a decrease in the column densities of Si II and C II, which is also seen in the observations. On the other hand, Si IV and C IV column densities would be expected to increase, but these cannot be confirmed as the corresponding troughs are saturated in both epochs. Therefore, our example shows that the observed pattern of variability could be due to changes in the ionization state of the gas.

6.2. Previous high-resolution studies of FeLoBAL outflows.

In section 4, we highlighted the importance of taking into account the physical structure of the cloud while estimating its n_H from the n_e determined from observed excited states of low-ionization species such as Fe II. Depending on parameters such as the thickness of the cloud, n_e/n_H can take values much lower than 1.2. The assumption of the plasma being highly ionized can then lead to an overestimation for the distance of the outflow (R) and its energetics (see eqn. 5 and 8).

Among the previous high-resolution studies of FeLoBAL outflows with distance determination, we found four such cases in which the effect of the physical structure of the cloud was not considered in their density diagnostics. For each of these objects, we model their outflowing cloud using the N_H , U_H and the incident SED prescribed in the respective analyzes. We then run a grid of models with varying n_H to find the value for which the weighted n_e matches the value determined using excited state ratios observed in their outflow system. Using this new n_H , we then reevaluate R , \dot{M} and \dot{E}_k for the outflows. Table 4 shows the result of this analysis. For three of these objects, the reevaluated distance determination does not vary significantly from the reported distance. However, for the outflow in J1321-0041, we find that $n_e/n_H \lesssim 10^{-1}$ and therefore the distance of the outflow from the central source was overestimated by $\sim 300\%$.

7. Summary and Conclusion

We have identified several outflow systems in the VLT/UVES spectrum of quasar SDSS J0932+0840, and analyze in detail the system with $v \sim -720 \text{ km s}^{-1}$.

1. In section 3.1 we outline our determination of the column densities of several ionic species. This enables us to employ photoionization modeling (see Fig. 5) for the outflow and obtain its total hydrogen column density ($\log N_H = 21.47^{+0.17}_{-0.16} \text{ [cm}^{-2}\text{]}$) and ionization parameter ($\log U_H = -2.4^{+0.4}_{-0.5}$).
2. The detection of several ground and excited state transitions of Fe II allow us to obtain the number density of the out-

flow. We model the electron number density (n_e) and hydrogen number density (n_H) independently and obtain $\log(n_e) = 3.42^{+0.65}_{-0.46} \text{ [cm}^{-3}\text{]}$ (section 4.1) and $\log(n_H) = 4.80 \text{ [cm}^{-3}\text{]}$ (section 4.2).

3. We take a deeper look into the physical structure of the cloud in section 4.3 and show that the formation of Fe II is subject to a different set of conditions than most of the cloud, as it takes place beyond the hydrogen ionization front, where n_e and temperature drop suddenly (see Fig. 8). Therefore for FeLoBAL outflows the approximation of highly ionized plasma doesn't hold as $n_e \neq 1.2n_H$.
4. We obtain the effective n_e for our modeled cloud with $\log(n_H) = 4.80 \text{ [cm}^{-3}\text{]}$ as $\log(n_{e,eff}) = 3.51 \text{ [cm}^{-3}\text{]}$. This is in agreement with the measured value of $\log(n_e) = 3.42^{+0.65}_{-0.46} \text{ [cm}^{-3}\text{]}$, and we thus show that our independent solutions for n_e and n_H are consistent with each other.
5. Using our obtained solution for n_H , we estimate the distance of the outflow to be $0.7^{+0.9}_{-0.4} \text{ kpc}$ from the central source. This leads to $\dot{M} = 43^{+65}_{-26} M_\odot \text{ yr}^{-1}$ and $\dot{E}_k = 0.7^{+1.1}_{-0.4} \times 10^{43} \text{ erg s}^{-1}$, with $\dot{E}_k/L_{Edd} = 0.5^{+0.7}_{-0.3} \times 10^{-4}$. This outflow is thus not expected to contribute significantly to AGN feedback.
6. We compare two epochs of SDSS spectra separated by ~ 2.4 years in the quasar rest frame and explain the observed pattern of absorption variation in terms of a change in the ionization state of the gas.

Acknowledgements. We acknowledge support from NSF grant AST 2106249, as well as NASA STScI grants AR-15786, AR-16600, AR-16601 and AR-17556.

References

- Arav, N., Borguet, B., Chamberlain, C., Edmonds, D., & Danforth, C. 2013, MNRAS, 436, 3286
- Arav, N., Brotherton, M. S., Becker, R. H., et al. 2001a, ApJ, 546, 140
- Arav, N., Chamberlain, C., Kriss, G., et al. 2015, A&A, 577, A37
- Arav, N., De Kool, M., Korista, K. T., et al. 2001b, ApJ, 561, 118
- Arav, N., Kaastra, J., Kriss, G. A., et al. 2005, ApJ, 620, 665
- Arav, N., Liu, G., Xu, X., et al. 2018, ApJ, 857, 60
- Arav, N., Moe, M., Costantini, E., et al. 2008, ApJ, 681, 954
- Badnell, N. 2011, Computer Physics Communications, 182, 1528
- Bahk, H., Woo, J.-H., & Park, D. 2019, ApJ, 875, 50
- Barlow, R. 2004, arXiv preprint physics/0401042
- Bautista, M. A., Dunn, J. P., Arav, N., et al. 2010, ApJ, 713, 25
- Bautista, M. A., Peng, J., & Pradhan, A. K. 1996, ApJ v. 460, p. 372, 460, 372
- Begelman, M. C. & Nath, B. B. 2005, MNRAS, 361, 1387
- Begelman, M. C. & Ruszkowski, M. 2005, Philosophical Transactions of the Royal Society of London Series A, 363, 655
- Borguet, B. C., Edmonds, D., Arav, N., Dunn, J., & Kriss, G. A. 2012, ApJ, 751, 107
- Brüggen, M. & Scannapieco, E. 2009, MNRAS, 398, 548
- Byun, D., Arav, N., & Hall, P. B. 2022a, ApJ, 927, 176
- Byun, D., Arav, N., & Hall, P. B. 2022b, MNRAS, 517, 1048
- Byun, D., Arav, N., Sharma, M., Dehghanian, M., & Walker, G. 2024a, A&A, 684, A158
- Byun, D., Arav, N., Sharma, M., Dehghanian, M., & Walker, G. 2024b, A&A, 684, A158
- Byun, D., Arav, N., & Walker, A. 2022c, MNRAS, 516, 100
- Capellupo, D. M., Hamann, F., Shields, J. C., Halpern, J. P., & Barlow, T. A. 2013, MNRAS, 429, 1872
- Chatzikos, M., Bianchi, S., Camilloni, F., et al. 2023, RMxAA, 59, 327
- Chen, C., Hamann, F., Ma, B., & Murphy, M. 2021, ApJ, 907, 84
- Choi, E., Ostriker, J. P., Naab, T., et al. 2017, ApJ, 844, 31
- Choi, H., Leighly, K. M., Dabbieri, C., et al. 2022a, ApJ, 936, 110
- Choi, H., Leighly, K. M., Terndrup, D. M., et al. 2022b, ApJ, 937, 74
- Choi, H., Leighly, K. M., Terndrup, D. M., Gallagher, S. C., & Richards, G. T. 2020, ApJ, 891, 53
- Ciotti, L., Ostriker, J. P., Gan, Z., et al. 2022, ApJ, 933, 154
- Cochrane, R., Anglés-Alcázar, D., Mercedes-Feliz, J., et al. 2023, MNRAS, 523, 2409
- Dai, X., Shankar, F., & Sivakoff, G. R. 2012, ApJ, 757, 180
- de Kool, M., Arav, N., Becker, R. H., et al. 2001, ApJ, 548, 609

Table 4: Re-evaluated density, distance and energetics for some FeLoBAL outflows from literature.

Object	$\log(N_H)$ [cm ⁻²]	$\log(U_H)$	$\log(n_H)$ [cm ⁻³]	v km s ⁻¹	R_{old}^a kpc	R_{new}^b kpc	\dot{M} $M_\odot \text{ yr}^{-1}$	$\log \dot{E}_k$ ergs s ⁻¹
J2357-0048 ¹	18.96 ^{+1.05} _{-0.64}	-3.76 ^{+0.88} _{-0.77}	4.32 ^{+0.2} _{-0.2}	-1600	10.90 ^{+16.6} _{-7.1}	9.30 ^{+14.0} _{-6.0}	3800 ⁺⁹⁶⁰⁰⁰ ₋₃₂₀₀ ^c	45.49 ^{+1.47} _{-0.85}
J0242+0049 ²	21.27 ^{+0.64} _{-0.58}	-1.30 ^{+0.49} _{-0.48}	0.21 ^{+0.21} _{-0.20}	-1800	67 ⁺⁵⁵ ₋₃₁	65 ⁺⁵³ ₋₃₀	6300 ⁺¹²⁰⁰⁰ ₋₃₆₀₀	45.81 ^{+0.47} _{-0.37}
J1439-0106 ³	20.99 ^{+0.61} _{-0.59}	-1.99 ^{+0.60} _{-0.58}	3.72 ^{+0.1} _{-0.1}	-1550	2.60 ^{+2.50} _{-1.3}	1.71 ^{+1.20} _{-1.07}	70 ⁺¹⁴⁰ ₋₅₀	43.75 ^{+0.45} _{-0.50}
J1321-0041 ⁴	21.73 ^{+0.39} _{-0.26}	-1.74 ^{+0.69} _{-0.27}	4.56 ^{+0.26} _{-0.20}	-4100	2.50 ^{+1.00} _{-1.40}	0.64 ^{+0.31} _{-0.37}	400 ⁺⁶⁸⁰ ₋₂₆₀	45.34 ^{+0.424} _{-0.451}

Notes. (a) Distance reported in the original work. (b) Reevaluated distance. (c) The energetics is for the higher ionization phase of the outflow, whereas the density was obtained from the low ionization phase.

References: (1) [Byun et al. \(2022b\)](#), (2) [Byun et al. \(2022a\)](#), (3) [Byun et al. \(2022c\)](#), (4) [Byun et al. \(2024b\)](#)

- de Kool, M., Becker, R. H., Arav, N., Gregg, M. D., & White, R. L. 2002a, *ApJ*, 570, 514
- de Kool, M., Becker, R. H., Gregg, M. D., White, R. L., & Arav, N. 2002b, *ApJ*, 567, 58
- de Kool, M., Korista, K. T., & Arav, N. 2002c, *ApJ*, 580, 54
- Dere, K., Landi, E., Mason, H., Fossi, B. M., & Young, P. 1997, *A&A Supplement Series*, 125, 149
- Dere, K. P., Del Zanna, G., Young, P. R., Landi, E., & Sutherland, R. S. 2019, *ApJ Supplement Series*, 241, 22
- Di Matteo, T., Springel, V., & Hernquist, L. 2005, *Nature*, 433, 604
- Dunn, J. P., Bautista, M., Arav, N., et al. 2010, *ApJ*, 709, 611
- Edmonds, D., Borguet, B., Arav, N., et al. 2011, *ApJ*, 739, 7
- Elvis, M. 2000, *ApJ*, 545, 63
- Fabjan, D., Borgani, S., Tornatore, L., et al. 2010, *MNRAS*, 401, 1670
- Gallagher, S., Brandt, W., Chartas, G., et al. 2006, *ApJ*, 644, 709
- Ganguly, R. & Brotherton, M. S. 2008, *ApJ*, 672, 102
- Green, P. J., Aldcroft, T. L., Mathur, S., Wilkes, B. J., & Elvis, M. 2001, *ApJ*, 558, 109
- Hall, P. B., Anderson, S. F., Strauss, M. A., et al. 2002, *ApJ Supplement Series*, 141, 267
- Hall, P. B., Anosov, K., White, R., et al. 2011, *MNRAS*, 411, 2653
- Hamann, F. & Sabra, B. 2004, in *Astronomical Society of the Pacific Conference Series*, Vol. 311, AGN Physics with the Sloan Digital Sky Survey, 203
- Hewett, P. C. & Foltz, C. B. 2003, *AJ*, 125, 1784
- Hidalgo, P. R., Hamann, F., Eracleous, M., et al. 2012, arXiv preprint arXiv:1203.3830
- Hopkins, P. F. & Elvis, M. 2010, *MNRAS*, 401, 7
- Hopkins, P. F., Murray, N., & Thompson, T. A. 2009, *MNRAS*, 398, 303
- Hopkins, P. F., Torrey, P., Faucher-Giguère, C.-A., Quataert, E., & Murray, N. 2016, *MNRAS*, 458, 816
- Knigge, C., Scaringi, S., Goad, M. R., & Cottis, C. E. 2008, *MNRAS*, 386, 1426
- Korista, K. T., Bautista, M. A., Arav, N., et al. 2008, *ApJ*, 688, 108
- Krolik, J. & Kriss, G. 1996, *ApJ* v. 456, p. 909, 456, 909
- Kurucz, R. & Bell, B. 1995, *Atomic Line Data (RL Kurucz and B. Bell) Kurucz CD-ROM No. 23*. Cambridge, 23
- Leighly, K. M., Choi, H., DeFrancesco, C., et al. 2022, *ApJ*, 935, 92
- Leighly, K. M., Terndrup, D. M., Gallagher, S. C., Richards, G. T., & Dietrich, M. 2018, *ApJ*, 866, 7
- Liao, S., Irodotou, D., Johansson, P. H., et al. 2024, *MNRAS*, stae1123
- Lucy, A. B., Leighly, K. M., Terndrup, D. M., Dietrich, M., & Gallagher, S. C. 2014, *ApJ*, 783, 58
- Lucy, L. 1995, *A&A (ISSN 0004-6361)*, vol. 294, no. 2, p. 555-567, 294, 555
- Moe, M., Arav, N., Bautista, M. A., & Korista, K. T. 2009, *ApJ*, 706, 525
- Moll, R., Schindler, S., Domainko, W., et al. 2007, *A&A*, 463, 513
- Morabito, L. K., Dai, X., Leighly, K. M., Sivakoff, G. R., & Shankar, F. 2011, *ApJ*, 737, 46
- Moravec, E., Hamann, F., Capellupo, D., et al. 2017, *MNRAS*, 468, 4539
- Morgan, C. W., Kochanek, C., Morgan, N. D., & Falco, E. E. 2010, *ApJ*, 712, 1129
- Murphy, M. T., Kacprzak, G. G., Savorgnan, G. A., & Carswell, R. F. 2019, *MNRAS*, 482, 3458
- Murray, N., Chiang, J., Grossman, S., & Voit, G. 1995, *ApJ* v. 451, p. 498, 451, 498
- Osterbrock, D. E. & Ferland, G. J. 2006, *Astrophysics Of Gas Nebulae and Active Galactic Nuclei (University science books)*
- Ostriker, J. P., Choi, E., Ciotti, L., Novak, G. S., & Proga, D. 2010, *ApJ*, 722, 642
- Peebles, P. 1972, *ApJ*, Vol. 178, pp. 371-376 (1972), 178, 371
- Peterson, B. M. 1997, *An introduction to active galactic nuclei (Cambridge University Press)*
- Planck Collaboration, Aghanim, N., Akrami, Y., et al. 2020, *A&A*, 641, A6
- Reichard, T. A., Richards, G. T., Hall, P. B., et al. 2003, *AJ*, 126, 2594
- Savage, B. D. & Sembach, K. R. 1991, *ApJ*, 379, 245
- Silk, J. & Rees, M. J. 1998, *A&A*, 331, L1
- Stone, R. B. & Richards, G. T. 2019, *MNRAS*, 488, 5916
- Trump, J. R., Hall, P. B., Reichard, T. A., et al. 2006, *ApJ Supplement Series*, 165, 1
- Vestergaard, M. 2003, *ApJ*, 599, 116
- Voit, G. M., Weymann, R. J., & Korista, K. T. 1993, *ApJ*, 413, 95
- Walker, A., Arav, N., & Byun, D. 2022, *MNRAS*, 516, 3778
- Weinberger, R., Su, K.-Y., Ehlert, K., et al. 2023, *MNRAS*, 523, 1104
- Weymann, R. J., Morris, S. L., Foltz, C. B., & Hewett, P. C. 1991, *ApJ*, Part 1 (ISSN 0004-637X), vol. 373, May 20, 1991, p. 23-53., 373, 23
- Xu, X., Arav, N., Miller, T., & Bunn, C. 2018, *ApJ*, 858, 39
- Xu, X., Arav, N., Miller, T., Korista, K. T., & Bunn, C. 2021, *MNRAS*, 506, 2725
- Yi, W., Brandt, W., Hall, P., et al. 2019, *ApJ Supplement Series*, 242, 28

Appendix A: Error estimation for mean n_e

We observed various excited states of Fe II in the system S2 of the outflow. Using the methodology described in Section 4.1, we obtained a corresponding electron number density (n_e) solution and its errors for each level as shown in Table A.1. To characterize the outflow with a single n_e , we obtain the weighted mean using the methodology described by Barlow (2004). To obtain an estimate for the error on the weighted mean, we use two different procedures, which are described below.

Table A.1: n_e obtained from CHIANTI for different Fe II level ratios

Energy Level (cm^{-1})	$\log(n_e)$ [cm^{-3}]
385	$3.1^{+0.4}_{-0.35}$
668	$3.75^{+0.5}_{-0.4}$
863	$3.75^{+0.55}_{-0.4}$
977	$3.5^{+0.55}_{-0.45}$
1873	$3.25^{+0.7}_{-0.5}$
Weighted Mean	3.42

Appendix A.1: Propagating errors associated with each measurement

One way to estimate error for the mean is to obtain the mean of the weighted errors added in quadrature. If the positive/negative error for the i^{th} measurement of x (x_i) is denoted as $(\delta x_i)^\pm$, then the positive/negative error for the mean, $(\delta \langle x \rangle)^\pm$, can be obtained as:

$$(\delta \langle x \rangle)^\pm = \frac{\sum \sqrt{w_i \cdot (\delta x_i)^\pm}}{\sum w_i} \quad (\text{A.1})$$

where w_i is the weight associated with each measurement as described in Barlow (2004). With $x = \log(n_e)$, we obtain $(\delta \langle \log(n_e) \rangle)^+ = 0.24$ and $(\delta \langle \log(n_e) \rangle)^- = 0.14$, and therefore we have $\langle \log(n_e) \rangle = 3.42^{+0.24}_{-0.19}$. While this is a robust method to take into account the errors associated with each measurement, it does not include information about the scatter in the values between measurements obtained from the different levels.

Appendix A.2: Standard Deviation including the measurement errors

To obtain errors on the mean in a way which includes the spread of the measurements around it, and also their own individual errors, we define:

$$(\delta \langle x \rangle)^\pm = \sqrt{\frac{\sum (\langle x \rangle - (x_i \pm (\delta x_i)^\pm))^2}{N}} \quad (\text{A.2})$$

where N is the total number of measurements and $\langle x \rangle$ is their mean. With $x = \log(n_e)$, this definition leads to $(\delta \langle \log(n_e) \rangle)^+ = 0.65$ and $(\delta \langle \log(n_e) \rangle)^- = 0.46$, and therefore we have $\langle \log(n_e) \rangle = 3.42^{+0.65}_{-0.46}$. We adopt this value for our analysis and represent it graphically in Fig. 6. It shows that given the scatter between the different measurements, eqn. (A.2) provides a much better representation of the error compared to the smaller values obtained from eqn. (A.1).